ACS APPLIED MATERIALS & INTERFACES

Research Article

www.acsami.org

Oxygen Evolution Catalyzed by Nickel–Iron Oxide Nanocrystals with a Nonequilibrium Phase

Jeremy A. Bau, Erik J. Luber,* and Jillian M. Buriak*

National Institute for Nanotechnology (NINT), National Research Council, 11421 Saskatchewan Drive, Edmonton, Alberta T6G 2M9, Canada

Department of Chemistry, University of Alberta, Edmonton, Alberta T6G 2G2, Canada

Supporting Information

ABSTRACT: Mixed nickel–iron oxides are of great interest as electrocatalysts for the oxygen evolution reaction (OER), the kinetically challenging half-reaction required for the generation of hydrogen gas from water via electrolysis. Previously, we had reported the synthesis of single crystal, soluble nickel–iron oxide nanoparticles over a wide range of nickel:iron compositions, with a metastable cubic rock salt phase ([Ni,Fe]O) that can be isolated despite the low solubility of iron in cubic nickel oxide at ambient temperatures. Here, activity for OER was examined, catalyzed by these [Ni,Fe]O nanoparticles integrated with indium tin oxide (ITO) electrodes. Because the as-prepared [Ni,Fe]O nanoparticles are oleate-capped, the surface ligands needed to be removed to induce adherence to the ITO substrate, and to enable charge transfer and contact with water to enable OER catalysis. Two different approaches were taken to reduce or eliminate the coverage of oleate ligands in these films: UV irradiation (254 nm) and air plasma. UV irradiation proved to lead to better results in terms of stable and OER-active films at pH 13. Kinetic analysis revealed that the Tafel slopes of these nanoparticle [Ni,Fe]O OER electrodes were limited by the electrochemical surface area and were found to be within the range of 30 to 50 mV/decade. Across the four compositions of Ni:Fe studied, from 24:76 to 88:12, the observed overpotential at 10 mA/cm^2 for the OER in basic conditions decreased from 0.47 to 0.30 V as the proportion of nickel increased from 24% to 88%.

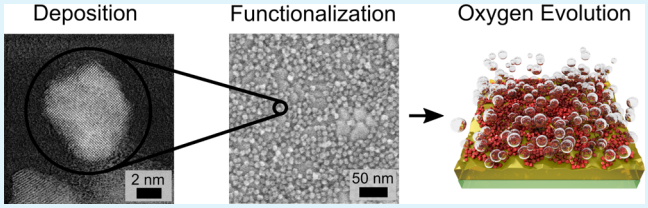

KEYWORDS: *water oxidation, oxygen evolution, nanocrystals, nonequilibrium, nickel oxide, iron oxide, electrolysis*

INTRODUCTION

An important requirement in the implementation of renewable energy is the development of energy storage systems; many renewable energy sources, particularly solar and wind power, are intermittent.[1−4] A number of storage options for energy derived from renewable sources are under consideration, including electrochemical storage (e.g., batteries, supercapacitors),[4,5] potential energy storage (e.g., hydroelectric dams, compressed air storage),[6,7] thermal storage (e.g., molten salt),[7,8] and many others. Chemical storage, however, offers the possibility of a direct fossil fuel replacement strategy since energy would be amassed in chemical bonds, as is the case for fossil fuels.[1,3] Examples of fuels for chemical storage of energy produced from renewable sources include hydrogen gas derived from the splitting of water,[9−13] and CO_2 conversion to methanol and hydrocarbons;[14−17] in these examples, the stored chemical energy could then be released through oxidation, such as direct combustion or via a fuel cell with oxygen.[18−20] Hydrogen is the cleanest fuel as it is entirely carbon neutral, producing only water upon combustion with oxygen.[1,3,9−13]

The direct electrolysis of water, powered by renewable energy sources, is of intense interest for the production of hydrogen gas.[1,3,9−13,21−23] Water electrolysis consists of the hydrogen and oxygen evolution half-reactions, each of which take place on separate electrodes. The hydrogen evolution reaction (HER) can be catalyzed with high efficiency by a variety of metal complexes,[24−28] metal surfaces,[29,30] metal chalcogenides,[31,32] metal phosphides,[33−35] and other metal-containing[36,37] as well as metal-free systems.[38] In contrast, the oxygen evolution reaction (OER) follows a more complex, multistep mechanism that requires the application of high overpotentials to enable the transfer of four electrons accompanying the decomposition of the water molecule or hydroxide ion.[3,10,39−41] If large-scale electrochemical hydrogen production is to become a reality, OER catalysts based on efficient, readily available materials are a necessity.

The utility of electrochemically active nickel and iron oxide systems for energy storage systems dates back over a century, when nickel–iron oxide batteries were independently invented by Edison and Jungner.[42−44] It was work on such battery systems that led to the serendipitous discovery that mixed nickel–iron oxide systems can catalyze the OER,[45,46] results that have been substantiated repeatedly over recent years via combinatorial screening and direct synthesis.[47−56] There are many variables within the nickel–iron oxide system to control, including composition, crystallinity, and oxidation states.

Received: June 23, 2015
Accepted: August 21, 2015
Published: August 21, 2015

DOI: 10.1021/acsami.5b05594
ACS Appl. Mater. Interfaces 2015, 7, 19755−19763

Recent work has shown that amorphous nickel−iron oxide materials with homogeneous compositions are highly active for OER catalysis under basic conditions,[48,49] while others have shown that ordered crystalline nanostructures, such as layered oxyhydroxide structures, are also highly active OER catalysts.[47,53,57−61] Small Fe(III)-doped rock salt NiO nanocrystals (sizes of 1.5−3.8 nm) on gold electrodes were shown to be active for OER catalysis, suggesting that nanocrystals could be a promising approach toward catalyst synthesis and development.[52] The influence and importance of crystallinity, or lack thereof, in nickel−iron oxide systems remains mostly unexplored and is worthy of further investigation to better understand the fundamental properties of active OER catalysts.

We previously reported the synthesis and characterization of ∼8 nm diameter single-crystal, mixed nickel−iron oxide nanoparticles with a rock salt phase, [Ni,Fe]O, and variable composition ratios of nickel to iron (Scheme 1), in which the

Scheme 1. Functionalization of ITO Electrodes with [Ni,Fe]O Nanoparticles

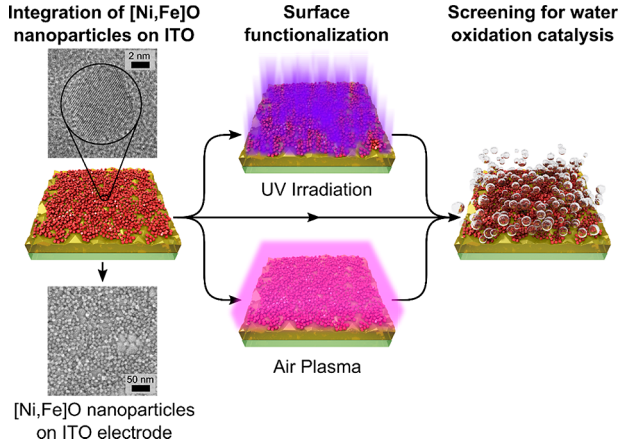

oxidation states of the nickel and iron are both in the +2 state in the nanoparticle core.[62] Electron energy loss spectroscopy (EELS), X-ray photoelectron spectroscopy (XPS), and magnetometry pointed to oxidation of surface iron species to trivalent Fe(III), along with Ni(II). Rock salt [Ni,Fe]O is normally an unstable phase at temperatures under 1073 K,[63,64] and thus, this metastable phase represents a new nickel−iron oxide phase for screening for OER activity. The ratio of Ni:Fe in the [Ni,Fe]O nanoparticle can be varied over a broad range from nickel rich, to iron rich, with no apparent change in crystal phase. In this work, we investigate the integration of these rock salt phase [Ni,Fe]O nanoparticles of varied Ni:Fe ratios with transparent indium tin oxide (ITO) electrodes, and carry out removal of surface ligands via two methods. These [Ni,Fe]O nanoparticles-on-ITO electrodes were screened for OER activity, longevity, and stability, and were shown to have overpotentials as low as 240 mV at 1 mA/cm^2, and 300 mV at 10 mA/cm^2. The effects of surface chemistry on longevity, the role of film thickness, and influence of the metastable [Ni,Fe]O rock salt phase on the OER were evaluated in order to determine the potential of this phase for applications in the electrolysis of water.

EXPERIMENTAL SECTION

Chemicals. $FeCl_3$ (98%) (Strem Chemicals), $NiCl_2{\cdot}6H_2O$ (ACP Chemicals), sodium oleate (>97%) (Tokyo Chemical Industry), ethanol (Commercial Alcohols), hexanes, acetonitrile, isopropanol, and potassium hydroxide (KOH, ACS Certified) (Fisher Chemicals), and 1,1′-ferrocenedicarboxylic acid ($Fc(COOH)_2$ 96%), oleic acid (technical grade, 90%), tetrabutylammonium hexafluorophosphate (TBAHFP, ≥ 99.0%), and 1-octadecene (technical grade, 90%) (Sigma-Aldrich) were used as received. Tin-doped indium oxide on glass (SiO_2 passivated, R_s = 8−12 Ω/□, "ITO") was acquired from Delta Technologies. Fluorine-doped tin oxide on glass (2 mm thickness, R_s ≈ 13 Ω/□, "FTO") was acquired from Pilkington via Sigma-Aldrich.

Nanoparticle Synthesis. All nanoparticles were synthesized as previously reported.[62] Briefly, metal chlorides in ratios of Ni:Fe 1:5, 2:4, 4:2, and 5:1 mmol were refluxed with sodium oleate amounting to 2 mmol of sodium oleate per mmol of Ni and 3 mmol of sodium oleate per mmol of Fe in a mixture of 20 mL of hexane, 10 mL of ethanol, and 10 mL of water at 60 °C for 4 h. After cooling, the hexane portion was separated and washed with water before centrifuging to remove more hydrophilic contaminants and products. The red-brown liquid was dried at 100 °C for 1 h in an oil bath in a fume hood to remove hexane. The waxy product was dissolved in 20 mL of 1-octadecene with 0.951 mL of oleic acid in a 250 mL three neck flask. The flask was degassed by evacuation and refilling three times with Ar at room temperature, and then at 110 °C. The reaction was then ramped to 305 °C at a rate of 3 °C/min and held at this temperature for 20 min. After cooling, 40 mL of isopropanol was added to the reaction mixture, which was then centrifuged and resuspended in hexane. Isopropanol was used to wash this mixture twice more before final storage in hexane under ambient conditions.

Electrode Fabrication. ITO and FTO substrates were diced into 2 cm × 2 cm squares, which were cleaned sequentially via sonication in methylene chloride, Milli-Q water (18.2 MΩ·cm), and isopropanol for 10 min each. Nanoparticle solutions in hexane diluted to 2 mg/mL were then spin-cast onto ITO and FTO surfaces 50 μL at a time and spun at 1000 rpm for 10 s. The nanoparticle-coated electrodes were then either left untreated, plasma-treated for 20 s under air plasma at 0.2 Torr (Harrick Plasma, PDC 32G, 18 W), or UV-irradiated for 1 h using a 254 nm Hg pen lamp (UVP) positioned 1 cm away from the surface of the electrode. For electrodes prepared with an oleate precursor (without nanoparticles), the precursor reflux solution described above was prepared with a ratio of Ni:Fe 3:3. The hexane layer was then separated and directly spin-cast onto ITO slides by applying 50 μL of the oleate mixture at a concentration of 100 mg/mL, and spinning at 1000 rpm for 10 s. The ITO slides with the oleate mixture were then irradiated for 1 h using 254 nm UV light.

Electrode Characterization. Imaging of the electrodes was performed using a Hitachi S-4800 FE-SEM instrument with an accelerating voltage of 20 kV, while thickness measurements were performed using a KLA Tencor P-10 surface profilometer. UV−vis measurements were performed using a PerkinElmer Lambda 1050 UV−vis NIR spectrophotometer. Energy dispersive X-ray (EDX) analysis of films fabricated from oleate precursors was performed on a JEOL JSM-6010LA InTouchScope.

Electrochemistry. All electrochemistry was performed using a Parstat 2273 potentiostat with Powersuite v2.58 software using a three-electrode electrochemical cell with a platinum wire counter electrode and an Ag/AgCl (saturated KCl) reference electrode standardized to potassium ferricyanide every time before testing. The working solution used for catalytic testing was 0.1 M KOH measured to be pH 12.8. Voltammetry scans measured from the open-circuit potential to a current density of 10 mA/cm^2, at a scan rate of 20 mV/s, were performed on all electrodes to ensure stability of recordings. Open circuit potential before all experiments was determined to lie between 0.0 and 0.1 V. The software used was PowerCV. Uncompensated resistance was determined using a Nyquist plot generated with POWERSine based on the left-side zero-intercept of the plot when imaginary resistance reached 0 Ω. Each point in the voltammogram was then corrected by subtracting from the potential the product of uncompensated resistance and current. Chronopotentiometry was undertaken using POWERStep software at a current density of 10 mA/cm^2. For Tafel plots, the current interrupt

DOI: 10.1021/acsami.5b05594
ACS Appl. Mater. Interfaces 2015, 7, 19755−19763

uncompensated resistance function was used as this option was available in the POWERCorr Tafel software. Tafel plots were taken at a rate of 10 mV/s with time steps of 50 s. This time was determined by chronoamperometry.

Electrochemically active surface area (ECSA) of electrodes of different layer numbers was determined using electrochemical impedance spectroscopy (EIS). ECSA was also indirectly measured based on charge transfer per surface area, as previously described, using the electrochemical adsorption of $Fc(COOH)_2$ to metal oxide surfaces.[65] The electrodes were plasma cleaned in air for 5 min to remove potential surface contaminants before immersion in 1 mM of 1,1′-ferrocenedicarboxylic acid in ethanol for 10 min. Afterward, the electrodes were washed with ethanol and acetonitrile. Cyclic voltammetry was then performed on the electrodes using an Ag/Ag^+ reference electrode in 0.1 M TBAHFP and acetonitrile. The scan range used was −0.50 to 1.75 V, at a rate of 0.10 V/s. The amount of charge transferred was taken by integrating the anodic peak in voltammograms using the Power Suite software.

Fourier Transform Infrared (FTIR) Spectroscopy. Scans were collected using a Nicolet Nexus 760 spectrometer with a DTGS detector and a N_2-purged sample chamber (256 scans, 4 cm^{-1} resolution). Nanoparticle samples were drop-cast on undoped, high resistivity (∼10 Ω·cm) Si wafers for data collection in transmission mode.

X-ray Photoelectron Spectroscopy. X-ray photoelectron spectroscopy (XPS) spectra were collected by an Kratos Ultra spectrometer with a base pressure less than 4×10^{-8} Pa. A monochromatic Al Kα source ($h\nu$ = 1486.6 eV) was run at a power of 168 W. The analysis spot was 300 μm × 700 μm, and the analyzer resolution was 0.80 eV for Au 4f peaks. The survey scans were collected for binding energies spanning 1100 to 0 eV at a constant energy of 160 eV and spectra for narrow regions were collected at a pass-energy of 20 eV. Sample charging was compensated by electron flooding. The binding energy (BE) scale was calibrated by assigning the C 1s peak from adventitious carbon at 284.8 eV. Relative concentrations of chemical elements were calculated using CasaXPS, using a standard quantification routine, including Scofield sensitivity factors and Shirley background subtraction.

X-ray Diffraction. X-ray diffraction (XRD) was performed using a Bruker D8 Discover instrument with a Cu Kα beam (40 kV, 40 mA, λ = 1.5406 Å) equipped with a 2D detector. XRD spectra were collected from the 2D ring patterns by chiral integration. Samples were prepared by drop-casting nanoparticle solution on silicon (100) substrates followed by heat treatment in air at either 200, 400, or 600 °C for 2 h in a Lindberg/Blue M tube furnace. Scans were performed in a grazing incidence configuration with an incident angle of $\omega = 5°$.

RESULTS AND DISCUSSION

Since the ultimate goal of this work was to determine the influence of the rock salt [Ni,Fe]O phase on OER catalysis, it was important that the chemical approaches used to functionalize and integrate the nanoparticles with the ITO electrodes did not result in deterioration of their crystallinity. The [Ni,Fe]O nanoparticles are capped with oleate ligands, which while imparting solubility to enable solution-phase processing, would likely impede electrochemical activity, and thus needs to be removed in part or entirely. Two different electrode functionalization approaches were examined, starting with spin-coating of films with a 2 mg/mL colloidal solution of [Ni,Fe]O nanoparticles in hexane on freshly cleaned ITO. In the first iteration, the [Ni,Fe]O nanoparticle-coated ITO electrode was subjected to a 20 s air plasma treatment at 0.2 Torr and 18 W ("plasma-treated"), while for the second, the electrode was irradiated with ultraviolet (254 nm, 15 mW UV pen lamp) light for 1 h ("UV-treated"), as outlined in Scheme 1. An "untreated" electrode refers to a [Ni,Fe]O nanoparticle-coated ITO electrode that has not been subjected to plasma or UV-irradiation. Air plasma treatment was selected because it has been shown to gently remove organic ligands with minimal changes to inorganic structures and surfaces,[66] while the efficacy of UV treatment at inducing the decomposition of 2-ethylhexanoate ligands of nickel and iron complexes was demonstrated by Berlinguette and co-workers.[22] Both approaches, plasma- and UV-treatments, led to similar UV−visible profiles (Supporting Information Figure S1), with an observable increase in the 350−500 nm range (Supporting Information Figure S2) as compared to bare ITO due to absorption by the [Ni,Fe]O nanoparticle films. The plasma treatment resulted in complete removal of oleate ligands, as determined by FTIR (Supporting Information Figure S3), and UV irradiation led to partial removal (vide infra).

The [Ni,Fe]O nanoparticle-ITO electrodes were then screened for OER activity via voltammetry under basic conditions, 0.1 M KOH (pH 12.8) at room temperature, as shown in Figure 1a. The potential of the electrodes was raised from open circuit potential until the current density reached at least 10 mA/cm^2, and then returned to open circuit potential, repeating this cycle until minimal change in overpotential was observed (Supporting Information Figure S4). The OER overpotential at 10 mA/cm^2 of UV-treated electrodes typically stopped changing after two or three cycles, while the OER overpotential for plasma-treated and untreated electrodes took up to 10 cycles to stabilize. UV-treated electrodes had the lowest overpotentials for OER (0.43 V) at a current density of 10 mA/cm^2 (Figure 1a), while plasma-treated electrodes had overpotentials of 0.60 V at the same current density. Meanwhile, untreated electrodes rapidly lost activity such that when the voltammograms finally reached stability, the voltammograms of the untreated electrodes appeared similar in catalytic activity to bare ITO. UV−vis studies of the electrodes post-voltammetry showed that the UV-treated electrodes maintained the same spectral profile, and had no change in absorption compared to an untreated electrode not used for voltammetry. In contrast, plasma-treated electrodes showed reduced absorption in the 350−500 nm region, while the untreated electrodes had a near-complete loss of absorption in this region when compared to an untreated electrode before voltammetry (Figure 1b). The stability of UV-treated electrodes was also studied by chronopotentiometry; under the stability testing criteria suggested by Jaramillo and co-workers of 10 mA/cm^2 for 2 h,[9] the UV-treated electrode demonstrated a 30 mV increase in overpotential, from 0.43 to 0.46 V (1.66 to 1.69 V vs RHE) (Figure 1c). The morphology of this nanoparticle film after stability testing, as per SEM inspection, was found to be mostly unchanged (Figure S5).

To determine what changes may have occurred during OER screening, untreated, plasma-treated, and UV-treated electrodes were examined using scanning electron microscopy (SEM), as shown in Figure 2, before and after ten cycles of voltammetry (cycles shown in the Supporting Information, Figure S4, where the electrode potential was raised until the current density reached at least 10 mA/cm^2 on the first cycle). SEM inspection of untreated nanoparticle electrodes ([Ni,Fe]O nanoparticles on ITO) showed the nanoparticle films are composed of uniformly distributed mats of nanoparticles with some regions of exposed ITO (Figure 2a). After voltammetry, the untreated electrode lost most of its nanoparticle coverage, and the surface looks like a sample of bare ITO (Figure 2b). Plasma treatment did not affect the initial appearance of electrodes before OER (Figure 2c), but after OER, more features indicative of the

DOI: 10.1021/acsami.5b05594
ACS Appl. Mater. Interfaces 2015, 7, 19755−19763

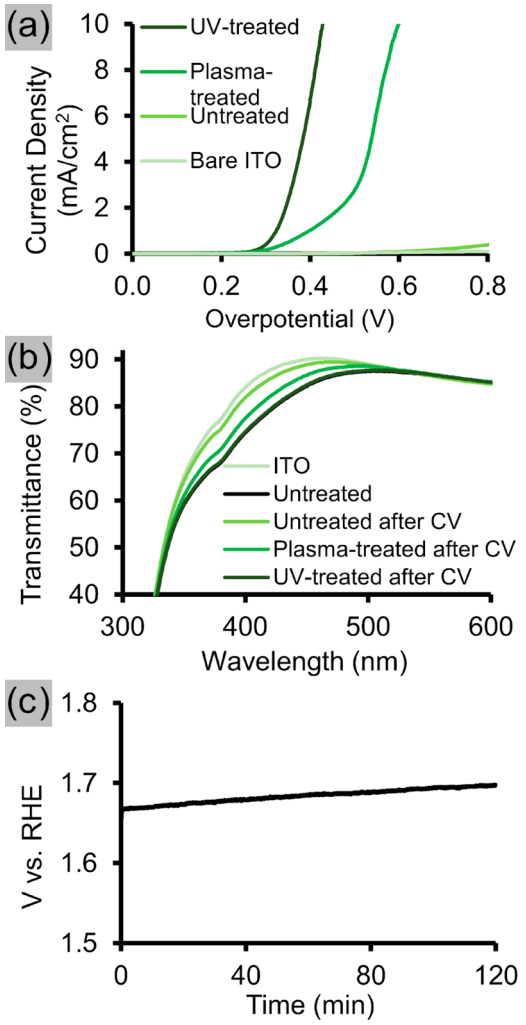

Figure 1. Catalytic and optical properties of ITO electrodes functionalized with Ni:Fe 51:49 [Ni,Fe]O nanoparticles via spin-coating, followed by 1 h of UV irradiation with 254 nm light (UV-treated), air plasma for 20 s (plasma-treated), and no further treatment (untreated) electrodes. (a) Voltammograms of UV-treated, plasma-treated, untreated electrodes, and a nanoparticle-free ITO control, in 0.1 M KOH. (b) UV−vis spectra of UV-treated, plasma-treated, and untreated [Ni,Fe]O electrodes before and after voltammetry as in (a). (c) Chronopotentiometry trace of UV-treated [Ni,Fe]O electrodes held at a current density of 10 mA/cm^2 for 2 h in 0.1 M KOH.

underlying ITO were visible, pointing to nanoparticle detachment (Figure 2d). Finally, UV-treated nanoparticle films were not visibly affected by the UV illumination treatment (Figure 2e), and remained similar in appearance after voltammetry (Figure 2f), suggesting that of the functionalization procedures attempted, only UV irradiation was successful at forming films of nanoparticles that could adhere in a stable manner to the ITO surface. A micrograph of bare ITO has been provided for comparison (Figure 2g). The data appear to support a claim that loss of catalytic activity and changes of UV−vis absoption profiles upon OER catalysis arose primarily from loss of nanoparticle coverage.

Since the UV-treatment appeared to be the most promising with respect to [Ni,Fe]O nanoparticle adhesion to the ITO and stability under OER conditions, this surface chemistry was examined in greater detail. FTIR of thin films of nanoparticles spin-cast on high-resistivity, native oxide-capped Si(100) was

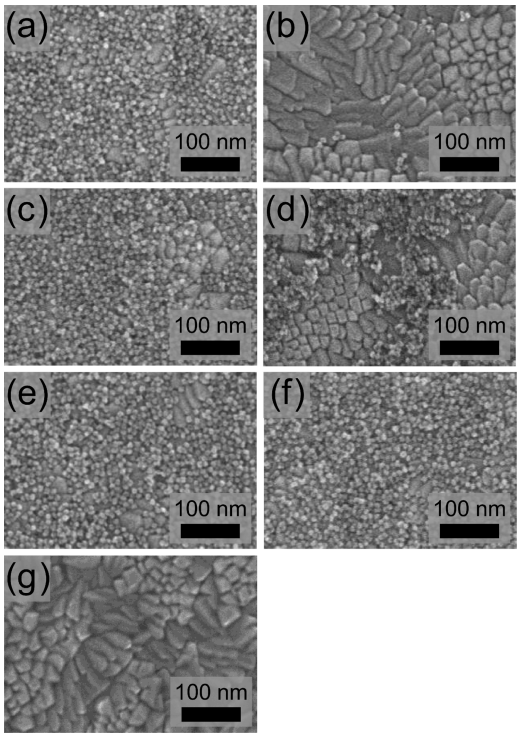

Figure 2. SEM micrographs of a Ni:Fe 51:49 [Ni,Fe]O-functionalized ITO electrode with no further treatment procedure (untreated) (a) before and (b) after voltammetry; a plasma-treated electrode (20 s, air) (c) before and (d) after voltammetry; and a UV-treated electrode (254 nm, 1 h) (e) before and (f) after voltammetry. (g) Micrograph of blank ITO.

used to determine the extent of removal of the oleate ligands by these treatments (Figure 3). The strongest feature, observed at

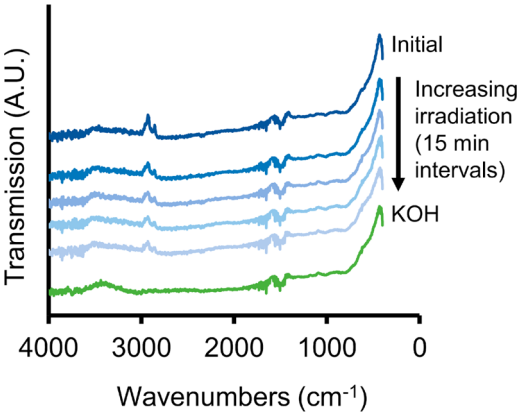

Figure 3. FTIR spectra of a Ni:Fe 51:49 [Ni,Fe]O nanoparticle film spun on high resistivity native oxide-capped Si(100) (~10 Ω·cm) after different periods of irradiation with 254 nm UV light, as well as after immersion in 0.1 M KOH for 2 h. Scans were collected transmission mode.

low energy, corresponds to modes associated with NiO (~450 cm^{-1}),[67,68] and FeO (410 cm^{-1}), and showed no change after 1 h of irradiation.[69] The $\nu(CH_x)$ region at 2800−3000 cm^{-1} diminished in intensity upon UV irradiation, corresponding to the photolytic decomposition of organic ligands. Decomposition of the oleate ligand was, however, incomplete after 1 h of irradiation as judged by the remaining features in the $\nu(CH_x)$

DOI: 10.1021/acsami.5b05594
ACS Appl. Mater. Interfaces 2015, 7, 19755−19763

region. Immersion in the highly basic aqueous solution used for OER catalysis, 0.1 M KOH, for 2 h resulted in the removal of all organic groups. Despite the lingering presence of ligand following UV irradiation, a shorter UV exposure time of 15 min appears to be sufficient to reach maximum OER activity, as shown by the results in Figure 4, comparing OER overpotentials at 10 mA/cm^2 for electrodes fabricated with irradiation times of 5, 10, 15, and 30 min.

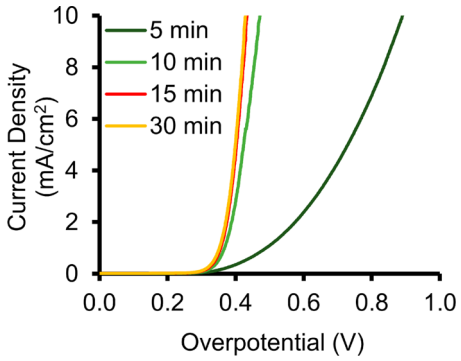

Figure 4. Voltammograms of Ni:Fe 51:49 [Ni,Fe]O nanoparticle-functionalized electrodes in 0.1 M KOH after irradiation with 254 nm UV light for different lengths of time.

To complement the FTIR surface analyses, X-ray photoelectron spectroscopy (XPS) of both the Ni 2p and Fe 3p regions was acquired; the spectra of untreated, UV-treated, UV-treated/0.1 M KOH-treated (2 h at open circuit potential in 0.1 M KOH), and UV-treated/postchronopotentiometry (10 mA/cm^2, 2 h) electrodes were contrasted, and no major differences in Fe 2p peak positions or shape were noted (Figure 5a). In the Ni 2p spectra, the position of the main peak at 854.5 eV remained constant under all examined conditions (Figure 5b), compared to the 3 eV shift previously reported for NiO that had been completely transformed from a cubic rock salt structure into a layered hydroxide structure.[57] XPS therefore suggests that, even under the harsh oxidizing conditions of the OER (0.1 M KOH, ~1.7 V vs RHE), the bivalency of the [Ni,Fe]O nanoparticles remained intact.

Given that the ratio of Ni:Fe is an important parameter in OER catalytic activity,[47−49,52,53] [Ni,Fe]O nanoparticles with different Ni:Fe ratios were also tested.[62] Hexane solutions of [Ni,Fe]O nanoparticles with Ni:Fe ratios of 88:12, 73:27, and 24:76 were spin-cast onto ITO electrodes and irradiated with UV light for 1 h, as carried out previously with the 51:49 [Ni,Fe]O nanoparticles (vide supra). Upon testing for OER catalysis in 0.1 M KOH, the electrodes were determined to have overpotentials of 0.32, 0.36, and 0.50 V, respectively, at a current density of 10 mA/cm^2 (Figure 6a). The overpotentials of these electrodes could be improved by increasing the quantity of [Ni,Fe]O nanoparticles on the surface via a layer-by-layer process of alternating spin-coating and UV irradiation. A modest reduction in overpotential was observed going from one to two layers of deposited [Ni,Fe]O nanoparticles, with the overpotential of Ni:Fe 24:76 being reduced from 0.50 to 0.47 V, Ni:Fe 51:49 being reduced from 0.44 to 0.40 V, the Ni:Fe 73:27 being reduced from 0.36 to 0.34 V, and the Ni:Fe 88:12 being reduced from 0.32 to 0.30 V (all parameters were kept equal and measured at a current density of 10 mA/cm^2, Figure 6b). However, additional layers did not significantly improve the observed overpotential. Therefore, the [Ni,Fe]O system

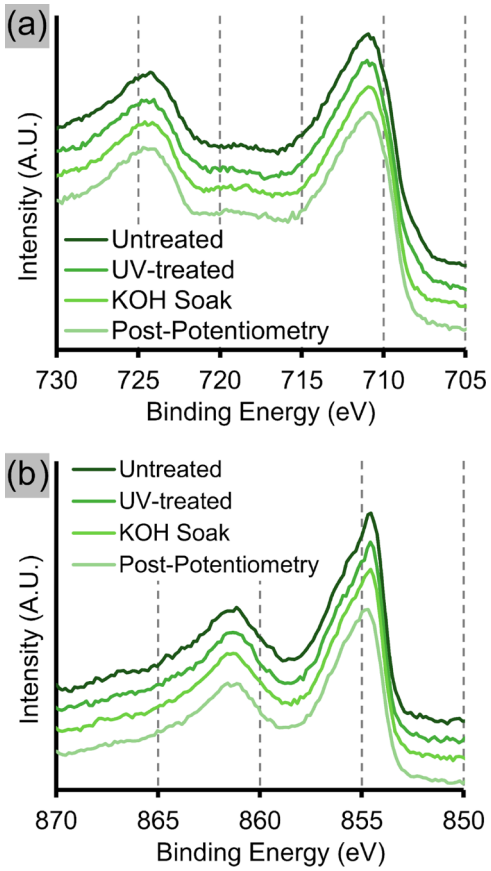

Figure 5. XPS spectra of the (a) Fe 2p and (b) Ni 2p$^{3/2}$ regions of a UV-treated Ni:Fe 51:49 [Ni,Fe]O nanoparticle-functionalized electrode before and after UV irradiation, after 2 h of immersion in electrolyte (0.1 M KOH), and postchronopotentiometry in 0.1 M KOH (10 mA/cm^2, 2 h).

reaches a minimal OER overpotential with two layers of [Ni,Fe]O nanoparticles, at a Ni:Fe ratio of 88:12, similar to other nickel−iron oxide systems.[47−49,53] Moreover, the magnitude of the measured overpotentials at 10 mA/cm^2 compares favorably to other planar nickel−iron oxide OER systems, which are typically found to have a minimum overpotential of ~0.3 V and are measured at pH = 14.[9,52,70] It is also noted that these nanoparticles could be well suited for recently developed methods of further reducing overpotential, where high surface area electrodes were fabricated by blending Ni−Fe sheets with graphene, resulting in overpotentials of ~0.26 V.[60,61] Lastly, these electrodes were all found to be stable under repeated electrochemical cycling (Figure S6).

To validate the claim of increasing thickness of the [Ni,Fe]O nanoparticle films on ITO, UV−vis spectroscopy was used to quantify the change in optical absorption with layer number (Figure 7a). Using the Ni:Fe 51:49 sample as an example, absorption increased monotonically with increasing layers of nanoparticles, reducing the transmission at 450 nm from 84.5% to 69.3% over the course of 4 layers cycles of spin-coating and UV irradiation. This increase in thickness was confirmed using profilometry, where the measured film thickness increased with the number of layers (Figure 7b). Single-layer nanoparticle films were not analyzed via this method because the films were incomplete. As determined by SEM, for all nanoparticles studied, a single cycle of nanoparticle deposition yielded incomplete nanoparticle films since bare ITO could be seen in

DOI: 10.1021/acsami.5b05594
ACS Appl. Mater. Interfaces 2015, 7, 19755−19763

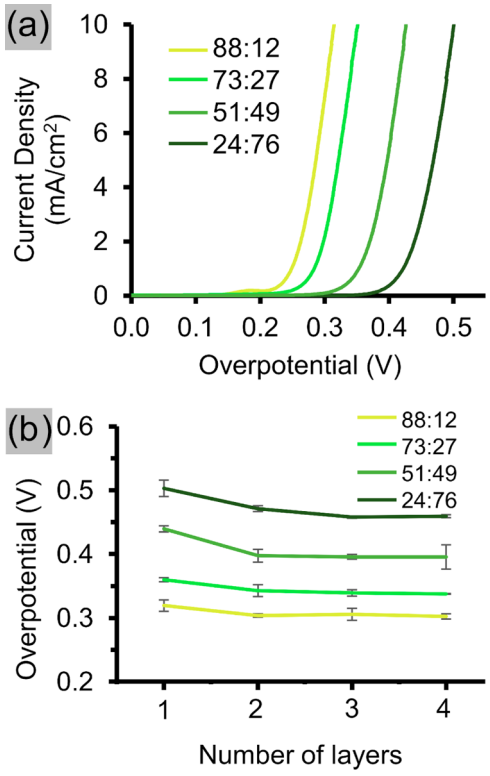

Figure 6. Catalytic properties of ITO electrodes functionalized with [Ni,Fe]O nanoparticles with compositions of Ni:Fe 88:12, 73:27, 51:49, and 24:76. (a) Voltammograms of [Ni,Fe]O nanoparticle-functionalized electrodes with one layer of nanoparticles of different compositions recorded in 0.1 M KOH. (b) Relationship of thickness based on number of layers and overpotential at 10 mA/cm^2 in 0.1 M KOH of different nanoparticle compositions. All ratios refer to Ni:Fe.

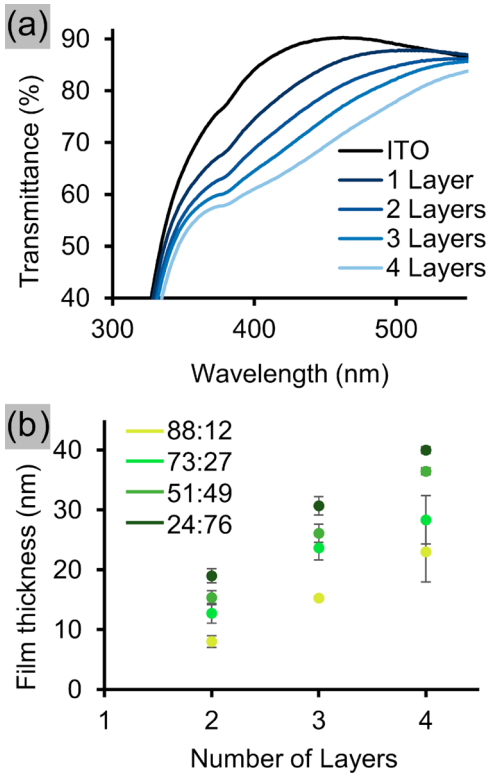

Figure 7. Optical and thickness properties of ITO electrodes functionalized with [Ni,Fe]O nanoparticles with compositions of Ni:Fe 88:12, 73:27, 51:49, and 24:76. (a) UV−vis spectra of [Ni,Fe]O nanoparticle-functionalized electrodes with increasing numbers of layers. The composition of nanoparticles used in this graph was Ni:Fe 51:49. (b) Relationship between thickness (determined via contact profilometry) and number of layers of [Ni,Fe]O nanoparticle-functionalized electrodes. All ratios refer to Ni:Fe.

some regions (Figure 8a,c,e,g). However, these regions disappeared after one additional loading cycle, resulting in continuous nanoparticle films with no visible ITO (Figure 8b,d,f,h). Since additional layers did not reduce the observed overpotential, it appears that surface coverage, not film thickness, was the most important factor in influencing overpotential. This result suggests that this method of layer-by-layer film deposition of these nanoparticles produces compact films, whereby subsequent layers bury underlying nanoparticles, making them inaccessible to the reactant molecules necessary for OER. In order to check this hypothesis, the ECSA of the electrodes was measured using EIS as a function of layer number. As shown in Figure S7, the ECSA is found to be constant (within error) as the number of layers is increased.

Tafel plots of the nanoparticle electrodes were acquired in order to study the kinetics of the OER on electrodes with two layers of nanoparticles, which had achieved the lowest overpotentials with the least catalyst material loading (Figure 9a). The Tafel slopes acquired from the [Ni,Fe]O nanoparticle electrodes in order of increasing slope values were 36 mV/decade (Ni:Fe 73:27), 42 mV/decade (Ni:Fe 88:12), 44 mV/decade (Ni:Fe 51:49), and 48 mV/decade (Ni:Fe 24:76) (Figure 9b), respectively. These values lie within the range of reported Tafel slopes for nickel−iron oxide catalysts, which are typically reported to lie between 30 and 50 mV/decade.[48−50] This suggests that the kinetics of the oxygen evolution reaction on the surfaces of these crystalline nanoparticles with a metastable rock salt phase is similar to other variations of Ni−Fe oxide OER catalysts.[71] In order to better understand this trend in Tafel slope as a function of nanoparticle film composition, the ECSA was measured. As seen in Figure 9b, we see that the Tafel slope has a strong inverse correlation with the ECSA; that is, as the ECSA is increased the Tafel slope decreases. As such, the OER kinetics of the [Ni,Fe]O nanoparticle electrodes are primarily governed by the available electrochemically active surface area.

It is also noted that the Tafel slope begins to increase at higher overpotentials (Figure 9a), which is generally observed in OER catalysis, and is typically attributed to either a change in the rate-determining step pathway or a change of the adsorption of OER intermediate species.[71] However, it is difficult to distinguish between these two scenarios for these data, since there is not a sharp transition between two distinct linear Tafel regions and it is also necessary to consider that increasing the amount of evolved gas can also reduce the effective surface area at higher potentials.[71]

The similar OER performance (overpotential and Tafel slope) of these rock salt phase nanoparticles to other Ni−Fe oxide catalysts can be better understood by analysis of the surface structure of these nanoparticles. Specifically, in our previous work,[62] it was shown through magnetometry and XPS that the surface of the nanoparticles consisted of a thin Ni−Fe oxide surface layer possessing Fe^{3+} species. Recent work by Friebel and co-workers[72] revealed that the active sites for Ni−

DOI: 10.1021/acsami.5b05594
ACS Appl. Mater. Interfaces 2015, 7, 19755−19763

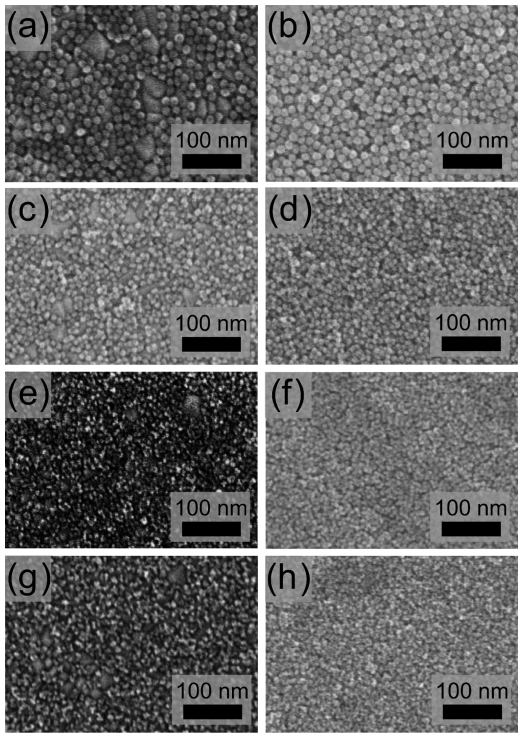

Figure 8. SEM micrographs of one layer (left) and two layer (right) nanoparticle electrodes with different compositions of nanoparticles. From top to bottom, the nanoparticle Ni:Fe compositions are 24:76 (a,b), 51:49 (c,d), 73:27 (e,f), and 88:12 (g,h).

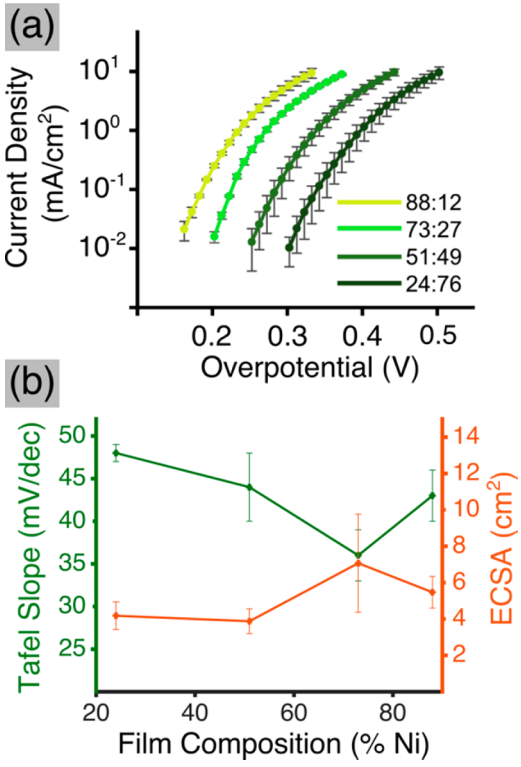

Figure 9. (a) Tafel curves of [Ni,Fe]O nanoparticle electrodes of different compositions acquired in 0.1 M KOH with 50 s step times. Ratios refer to Ni:Fe. (b) Tafel slopes at 0.5 mA/cm^2 and electrochemical surface area as measured by EIS.

Fe oxide OER catalysts comprise Fe^{3+} surface species, and *not* the nickel centers. As such, despite the inherently different crystal structure of these rock salt Ni−Fe oxide nanoparticles, the presence of Fe^{3+} species on the surface could account for the majority of the observed OER catalytic activity.

CONCLUSIONS

A metastable rock salt phase of single crystal [Ni,Fe]O nanoparticles was tested for oxygen evolution reaction (OER) catalysis; the Ni:Fe ratio could be synthetically controlled, from iron rich to nickel rich, with no change in crystal structure. These [Ni,Fe]O nanoparticles were integrated with an indium tin oxide (ITO) electrode via two chemical approaches, the first involving plasma treatment, and the second utilizing UV irradiation. The UV irradiation deposited on electrode surfaces led to films that adhered to the ITO surface, and could be electrochemically cycled, and maintained at 10 mA/cm^2 for 2 h. The nickel-rich nanoparticles resulted in the lowest observed overpotential for the OER, of 300 mV at 10 mA/cm^2. Moreover, the Tafel slopes were found to be in the range of 36−48 mV/decade. It was proposed that the OER performance of the [Ni,Fe]O electrodes could be attributed to the active Fe^{3+} sites on the nanoparticle surfaces, while the OER kinetics were limited by electrochemical surface area. Lastly, these nanoparticle catalysts represent a promising candidate for the decoration of high surface area conductive scaffolds.

ASSOCIATED CONTENT

Supporting Information

The Supporting Information is available free of charge on the ACS Publications website at DOI: 10.1021/acsami.5b05594.

Discussion on effects of heating on the catalytic activity of [Ni,Fe]O electrodes and on the use of electrodes fabricated from metal oleate precursors, as well as additional CV traces, FTIR spectra, and UV−vis of [Ni,Fe]O electrodes (PDF)

AUTHOR INFORMATION

Corresponding Authors

*E-mail: jburiak@ualberta.ca.
*E-mail: eluber@ualberta.ca.

Notes

The authors declare no competing financial interest.

ACKNOWLEDGMENTS

This work was supported by the Natural Sciences and Engineering Research Council of Canada (NSERC − Fellowship to J.A.B., NSERC Discovery Grant RGPIN-2014-05195), and Alberta Innovates Technology Futures (AITF − Fellowship to J.A.B., AITF Industrial Chair IC50-T1). We would like to thank the Alberta Centre for Surface Engineering and Science (ACSES) for XPS analyses, and the National Institute for Nanotechnology (NRC-NINT) for assistance with TEM analyses. We thank Brian C. Olsen for assistance with the graphics.

REFERENCES

(1) Lewis, N. S.; Nocera, D. G. Powering the Planet: Chemical Challenges in Solar Energy Utilization. *Proc. Natl. Acad. Sci. U. S. A.* **2006**, *103*, 15729−15735.

DOI: 10.1021/acsami.5b05594
ACS Appl. Mater. Interfaces 2015, 7, 19755−19763

(2) Barton, J. P.; Infield, D. G. Energy Storage and Its Use with Intermittent Renewable Energy. *IEEE Trans. Energy Convers.* **2004**, *19*, 441−448.
(3) Cook, T. R.; Dogutan, D. K.; Reece, S. Y.; Surendranath, Y.; Teets, T. S.; Nocera, D. G. Solar Energy Supply and Storage for the Legacy and Nonlegacy Worlds. *Chem. Rev.* **2010**, *110*, 6474−6502.
(4) Yang, Z.; Zhang, J.; Kintner-Meyer, M. C. W.; Lu, X.; Choi, D.; Lemmon, J. P.; Liu, J. Electrochemical Energy Storage for Green Grid. *Chem. Rev.* **2011**, *111*, 3577−3613.
(5) Wang, G.; Zhang, L.; Zhang, J. A Review of Electrode Materials for Electrochemical Supercapacitors. *Chem. Soc. Rev.* **2012**, *41*, 797−828.
(6) Kosnik, L. The Potential of Water Power in the Fight against Global Warming in the US. *Energy Policy* **2008**, *36*, 3252−3265.
(7) Ibrahim, H.; Ilinca, A.; Perron, J. Energy Storage systems—Characteristics and Comparisons. *Renewable Sustainable Energy Rev.* **2008**, *12*, 1221−1250.
(8) Liu, C.; Li, F.; Ma, L.-P.; Cheng, H.-M. Advanced Materials for Energy Storage. *Adv. Mater.* **2010**, *22*, E28−E62.
(9) McCrory, C. C. L.; Jung, S.; Peters, J. C.; Jaramillo, T. F. Benchmarking Heterogeneous Electrocatalysts for the Oxygen Evolution Reaction. *J. Am. Chem. Soc.* **2013**, *135*, 16977−16987.
(10) Walter, M. G.; Warren, E. L.; McKone, J. R.; Boettcher, S. W.; Mi, Q.; Santori, E. A.; Lewis, N. S. Solar Water Splitting Cells. *Chem. Rev.* **2010**, *110*, 6446−6473.
(11) Mayer, M. T.; Lin, Y.; Yuan, G.; Wang, D. Forming Heterojunctions at the Nanoscale for Improved Photoelectrochemical Water Splitting by Semiconductor Materials: Case Studies on Hematite. *Acc. Chem. Res.* **2013**, *46*, 1558−1566.
(12) Bard, A. J.; Fox, M. A. Artificial Photosynthesis: Solar Splitting of Water to Hydrogen and Oxygen. *Acc. Chem. Res.* **1995**, *28*, 141−145.
(13) Han, Z.; Eisenberg, R. Fuel from Water: The Photochemical Generation of Hydrogen from Water. *Acc. Chem. Res.* **2014**, *47*, 2537−2544.
(14) Li, H.; Zhang, X.; MacFarlane, D. R. Carbon Quantum Dots/Cu_2O Heterostructures for Solar-Light-Driven Conversion of CO2 to Methanol. *Adv. Energy Mater.* **2015**, DOI: 10.1002/aenm.201401077.
(15) Barton, E. E.; Rampulla, D. M.; Bocarsly, A. B. Selective Solar-Driven Reduction of CO_2 to Methanol Using a Catalyzed p-GaP Based Photoelectrochemical Cell. *J. Am. Chem. Soc.* **2008**, *130*, 6342−6344.
(16) Mao, X.; Hatton, T. A. Recent Advances in Electrocatalytic Reduction of Carbon Dioxide Using Metal-Free Catalysts. *Ind. Eng. Chem. Res.* **2015**, *54*, 4033−4042.
(17) Appel, A. M.; Bercaw, J. E.; Bocarsly, A. B.; Dobbek, H.; DuBois, D. L.; Dupuis, M.; Ferry, J. G.; Fujita, E.; Hille, R.; Kenis, P. J. A.; Kerfeld, C. A.; Morris, R. H.; Peden, C. H. F.; Portis, A. R.; Ragsdale, S. W.; Rauchfuss, T. B.; Reek, J. N. H.; Seefeldt, L. C.; Thauer, R. K.; Waldrop, G. L. Frontiers, Opportunities, and Challenges in Biochemical and Chemical Catalysis of CO_2 Fixation. *Chem. Rev.* **2013**, *113*, 6621−6658.
(18) Chiang, Y.-C.; Chang, C.-T. Single-Objective and Multiobjective Designs for Hydrogen Networks with Fuel Cells. *Ind. Eng. Chem. Res.* **2014**, *53*, 6006−6020.
(19) Borup, R.; Meyers, J.; Pivovar, B.; Kim, Y. S.; Mukundan, R.; Garland, N.; Myers, D.; Wilson, M.; Garzon, F.; Wood, D.; Zelenay, P.; More, K.; Stroh, K.; Zawodzinski, T.; Boncella, J.; McGrath, J. E.; Inaba, M.; Miyatake, K.; Hori, M.; Ota, K.; Ogumi, Z.; Miyata, S.; Nishikata, A.; Siroma, Z.; Uchimoto, Y.; Yasuda, K.; Kimijima, K.-I.; Iwashita, N. Scientific Aspects of Polymer Electrolyte Fuel Cell Durability and Degradation. *Chem. Rev.* **2007**, *107*, 3904−3951.
(20) Bomgardner, M. M. Fuel-Cell Cars Start To Arrive. *Chem. Eng. News* **2014**, *92*, 17−20.
(21) Kanan, M. W.; Nocera, D. G. In Situ Formation of an Oxygen-Evolving Catalyst in Neutral Water Containing Phosphate and Co^{2+}. *Science* **2008**, *321*, 1072−1075.
(22) Smith, R. D. L.; Prévot, M. S.; Fagan, R. D.; Zhang, Z.; Sedach, P. A.; Siu, M. K. J.; Trudel, S.; Berlinguette, C. P. Photochemical Route for Accessing Amorphous Metal Oxide Materials for Water Oxidation Catalysis. *Science* **2013**, *340*, 60−63.
(23) Esswein, A. J.; Surendranath, Y.; Reece, S. Y.; Nocera, D. G. Highly Active Cobalt Phosphate and Borate Based Oxygen Evolving Catalysts Operating in Neutral and Natural Waters. *Energy Environ. Sci.* **2011**, *4*, 499−504.
(24) Eckenhoff, W. T.; Eisenberg, R. Molecular Systems for Light Driven Hydrogen Production. *Dalton Trans.* **2012**, *41*, 13004−13021.
(25) Han, Z.; McNamara, W. R.; Eum, M.-S.; Holland, P. L.; Eisenberg, R. A Nickel Thiolate Catalyst for the Long-Lived Photocatalytic Production of Hydrogen in a Noble-Metal-Free System. *Angew. Chem., Int. Ed.* **2012**, *51*, 1667−1670.
(26) McCrory, C. C. L.; Uyeda, C.; Peters, J. C. Electrocatalytic Hydrogen Evolution in Acidic Water with Molecular Cobalt Tetraazamacrocycles. *J. Am. Chem. Soc.* **2012**, *134*, 3164−3170.
(27) Jacques, P.-A.; Artero, V.; Pécaut, J.; Fontecave, M. Cobalt and Nickel Diimine-Dioxime Complexes as Molecular Electrocatalysts for Hydrogen Evolution with Low Overvoltages. *Proc. Natl. Acad. Sci. U. S. A.* **2009**, *106*, 20627−20632.
(28) Lazarides, T.; McCormick, T.; Du, P.; Luo, G.; Lindley, B.; Eisenberg, R. Making Hydrogen from Water Using a Homogeneous System Without Noble Metals. *J. Am. Chem. Soc.* **2009**, *131*, 9192−9194.
(29) Greeley, J.; Jaramillo, T. F.; Bonde, J.; Chorkendorff, I.; Nørskov, J. K. Computational High-Throughput Screening of Electrocatalytic Materials for Hydrogen Evolution. *Nat. Mater.* **2006**, *5*, 909−913.
(30) McKone, J. R.; Marinescu, S. C.; Brunschwig, B. S.; Winkler, J. R.; Gray, H. B. Earth-Abundant Hydrogen Evolution Electrocatalysts. *Chem. Sci.* **2014**, *5*, 865−878.
(31) Merki, D.; Hu, X. Recent Developments of Molybdenum and Tungsten Sulfides as Hydrogen Evolution Catalysts. *Energy Environ. Sci.* **2011**, *4*, 3878−3888.
(32) Kong, D.; Cha, J. J.; Wang, H.; Lee, H. R.; Cui, Y. First-Row Transition Metal Dichalcogenide Catalysts for Hydrogen Evolution Reaction. *Energy Environ. Sci.* **2013**, *6*, 3553−3558.
(33) Popczun, E. J.; McKone, J. R.; Read, C. G.; Biacchi, A. J.; Wiltrout, A. M.; Lewis, N. S.; Schaak, R. E. Nanostructured Nickel Phosphide as an Electrocatalyst for the Hydrogen Evolution Reaction. *J. Am. Chem. Soc.* **2013**, *135*, 9267−9270.
(34) Popczun, E. J.; Read, C. G.; Roske, C. W.; Lewis, N. S.; Schaak, R. E. Highly Active Electrocatalysis of the Hydrogen Evolution Reaction by Cobalt Phosphide Nanoparticles. *Angew. Chem.* **2014**, *126*, 5531−5534.
(35) Callejas, J. F.; McEnaney, J. M.; Read, C. G.; Crompton, J. C.; Biacchi, A. J.; Popczun, E. J.; Gordon, T. R.; Lewis, N. S.; Schaak, R. E. Electrocatalytic and Photocatalytic Hydrogen Production from Acidic and Neutral-pH Aqueous Solutions Using Iron Phosphide Nanoparticles. *ACS Nano* **2014**, *8*, 11101−11107.
(36) Vrubel, H.; Hu, X. Molybdenum Boride and Carbide Catalyze Hydrogen Evolution in Both Acidic and Basic Solutions. *Angew. Chem.* **2012**, *124*, 12875−12878.
(37) Chen, W.-F.; Muckerman, J. T.; Fujita, E. Recent Developments in Transition Metal Carbides and Nitrides as Hydrogen Evolution Electrocatalysts. *Chem. Commun.* **2013**, *49*, 8896−8909.
(38) Zheng, Y.; Jiao, Y.; Zhu, Y.; Li, L. H.; Han, Y.; Chen, Y.; Du, A.; Jaroniec, M.; Qiao, S. Z. Hydrogen Evolution by a Metal-Free Electrocatalyst. *Nat. Commun.* **2014**, *5*, 3783.
(39) McCrory, C. C. L.; Jung, S.; Ferrer, I. M.; Chatman, S. M.; Peters, J. C.; Jaramillo, T. F. Benchmarking Hydrogen Evolving Reaction and Oxygen Evolving Reaction Electrocatalysts for Solar Water Splitting Devices. *J. Am. Chem. Soc.* **2015**, *137*, 4347−4357.
(40) Betley, T. A.; Wu, Q.; Van Voorhis, T.; Nocera, D. G. Electronic Design Criteria for O−O Bond Formation via Metal−Oxo Complexes. *Inorg. Chem.* **2008**, *47*, 1849−1861.
(41) Dau, H.; Limberg, C.; Reier, T.; Risch, M.; Roggan, S.; Strasser, P. The Mechanism of Water Oxidation: From Electrolysis via Homogeneous to Biological Catalysis. *ChemCatChem* **2010**, *2*, 724−761.

DOI: 10.1021/acsami.5b05594
ACS Appl. Mater. Interfaces 2015, 7, 19755−19763

(42) Wang, H.; Liang, Y.; Gong, M.; Li, Y.; Chang, W.; Mefford, T.; Zhou, J.; Wang, J.; Regier, T.; Wei, F.; et al. An Ultrafast Nickel−iron Battery from Strongly Coupled Inorganic Nanoparticle/nanocarbon Hybrid Materials. *Nat. Commun.* **2012**, *3*, 917.
(43) Halpert, G. Past Developments and the Future of Nickel Electrode Cell Technology. *J. Power Sources* **1984**, *12*, 177−192.
(44) Chakkaravarthy, C.; Periasamy, P.; Jegannathan, S.; Vasu, K. I. The Nickel/iron Battery. *J. Power Sources* **1991**, *35*, 21−35.
(45) Corrigan, D. A. The Catalysis of the Oxygen Evolution Reaction by Iron Impurities in Thin Film Nickel Oxide Electrodes. *J. Electrochem. Soc.* **1987**, *134*, 377−384.
(46) Corrigan, D. A.; Bendert, R. M. Effect of Coprecipitated Metal Ions on the Electrochemistry of Nickel Hydroxide Thin Films: Cyclic Voltammetry in 1 M KOH. *J. Electrochem. Soc.* **1989**, *136*, 723−728.
(47) Trotochaud, L.; Young, S. L.; Ranney, J. K.; Boettcher, S. W. Nickel−Iron Oxyhydroxide Oxygen-Evolution Electrocatalysts: The Role of Intentional and Incidental Iron Incorporation. *J. Am. Chem. Soc.* **2014**, *136*, 6744−6753.
(48) Smith, R. D. L.; Prévot, M. S.; Fagan, R. D.; Trudel, S.; Berlinguette, C. P. Water Oxidation Catalysis: Electrocatalytic Response to Metal Stoichiometry in Amorphous Metal Oxide Films Containing Iron, Cobalt, and Nickel. *J. Am. Chem. Soc.* **2013**, *135*, 11580−11586.
(49) Qiu, Y.; Xin, L.; Li, W. Electrocatalytic Oxygen Evolution over Supported Small Amorphous Ni−Fe Nanoparticles in Alkaline Electrolyte. *Langmuir* **2014**, *30*, 7893−7901.
(50) Gerken, J. B.; Shaner, S. E.; Massé, R. C.; Porubsky, N. J.; Stahl, S. S. A Survey of Diverse Earth Abundant Oxygen Evolution Electrocatalysts Showing Enhanced Activity from Ni−Fe Oxides Containing a Third Metal. *Energy Environ. Sci.* **2014**, *7*, 2376−2382.
(51) Xiang, C.; Suram, S. K.; Haber, J. A.; Guevarra, D. W.; Soedarmadji, E.; Jin, J.; Gregoire, J. M. High-Throughput Bubble Screening Method for Combinatorial Discovery of Electrocatalysts for Water Splitting. *ACS Comb. Sci.* **2014**, *16*, 47−52.
(52) Fominykh, K.; Chernev, P.; Zaharieva, I.; Sicklinger, J.; Stefanic, G.; Döblinger, M.; Müller, A.; Pokharel, A.; Böcklein, S.; Scheu, C.; Bein, T.; Fattakhova-Rohlfing, D. Iron-Doped Nickel Oxide Nanocrystals as Highly Efficient Electrocatalysts for Alkaline Water Splitting. *ACS Nano* **2015**, *9*, 5180−5188.
(53) Landon, J.; Demeter, E.; İnoğlu, N.; Keturakis, C.; Wachs, I. E.; Vasić, R.; Frenkel, A. I.; Kitchin, J. R. Spectroscopic Characterization of Mixed Fe−Ni Oxide Electrocatalysts for the Oxygen Evolution Reaction in Alkaline Electrolytes. *ACS Catal.* **2012**, *2*, 1793−1801.
(54) Gong, M.; Dai, H. A Mini Review of NiFe-Based Materials as Highly Active Oxygen Evolution Reaction Electrocatalysts. *Nano Res.* **2015**, *8*, 23−39.
(55) Schäfer, H.; Sadaf, S.; Walder, L.; Kuepper, K.; Dinklage, S.; Wollschläger, J.; Schneider, L.; Steinhart, M.; Hardege, J.; Daum, D. Stainless Steel Made to Rust: A Robust Water-Splitting Catalyst with Benchmark Characteristics. *Energy Environ. Sci.* **2015**, DOI: 10.1039/C5EE01601K.
(56) Schäfer, H.; Beladi-Mousavi, S. M.; Walder, L.; Wollschläger, J.; Kuschel, O.; Ichilmann, S.; Sadaf, S.; Steinhart, M.; Küpper, K.; Schneider, L. Surface Oxidation of Stainless Steel: Oxygen Evolution Electrocatalysts with High Catalytic Activity. *ACS Catal.* **2015**, *5*, 2671−2680.
(57) Trotochaud, L.; Ranney, J. K.; Williams, K. N.; Boettcher, S. W. Solution-Cast Metal Oxide Thin Film Electrocatalysts for Oxygen Evolution. *J. Am. Chem. Soc.* **2012**, *134*, 17253−17261.
(58) Tang, D.; Liu, J.; Wu, X.; Liu, R.; Han, X.; Han, Y.; Huang, H.; Liu, Y.; Kang, Z. Carbon Quantum Dot/NiFe Layered Double-Hydroxide Composite as a Highly Efficient Electrocatalyst for Water Oxidation. *ACS Appl. Mater. Interfaces* **2014**, *6*, 7918−7925.
(59) Feng, Y.; Zhang, H.; Zhang, Y.; Li, X.; Wang, Y. Ultrathin Two-Dimensional Free-Standing Sandwiched NiFe/C for High-Efficiency Oxygen Evolution Reaction. *ACS Appl. Mater. Interfaces* **2015**, *7*, 9203−9210.
(60) Yu, X.; Zhang, M.; Yuan, W.; Shi, G. A High-Performance Three-Dimensional Ni−Fe Layered Double Hydroxide/graphene Electrode for Water Oxidation. *J. Mater. Chem. A* **2015**, *3*, 6921−6928.
(61) Ma, W.; Ma, R.; Wang, C.; Liang, J.; Liu, X.; Zhou, K.; Sasaki, T. A Superlattice of Alternately Stacked Ni−Fe Hydroxide Nanosheets and Graphene for Efficient Splitting of Water. *ACS Nano* **2015**, *9*, 1977−1984.
(62) Bau, J. A.; Li, P.; Marenco, A. J.; Trudel, S.; Olsen, B. C.; Luber, E. J.; Buriak, J. M. Nickel/Iron Oxide Nanocrystals with a Nonequilibrium Phase: Controlling Size, Shape, and Composition. *Chem. Mater.* **2014**, *26*, 4796−4804.
(63) Rhamdhani, M. A.; Hayes, P. C.; Jak, E. Subsolidus Phase Equilibria of the Fe-Ni-O System. *Metall. Mater. Trans. B* **2008**, *39*, 690−701.
(64) Mallick, P.; Rath, C.; Biswal, R.; Mishra, N. C. Structural and Magnetic Properties of Fe Doped NiO. *Indian J. Phys.* **2009**, *83*, 517−523.
(65) Krause, K. M.; Taschuk, M. T.; Harris, K. D.; Rider, D. A.; Wakefield, N. G.; Sit, J. C.; Buriak, J. M.; Thommes, M.; Brett, M. J. Surface Area Characterization of Obliquely Deposited Metal Oxide Nanostructured Thin Films. *Langmuir* **2010**, *26*, 4368−4376.
(66) Gehl, B.; Frömsdorf, A.; Aleksandrovic, V.; Schmidt, T.; Pretorius, A.; Flege, J.-I.; Bernstorff, S.; Rosenauer, A.; Falta, J.; Weller, H.; Bäumer, M. Structural and Chemical Effects of Plasma Treatment on Close-Packed Colloidal Nanoparticle Layers. *Adv. Funct. Mater.* **2008**, *18*, 2398−2410.
(67) Xia, X. H.; Tu, J. P.; Zhang, J.; Wang, X. L.; Zhang, W. K.; Huang, H. Electrochromic Properties of Porous NiO Thin Films Prepared by a Chemical Bath Deposition. *Sol. Energy Mater. Sol. Cells* **2008**, *92*, 628−633.
(68) Subramanian, B.; Mohamed Ibrahim, M.; Senthilkumar, V.; Murali, K. R.; Vidhya, V.; Sanjeeviraja, C.; Jayachandran, M. Optoelectronic and Electrochemical Properties of Nickel Oxide (NiO) Films Deposited by DC Reactive Magnetron Sputtering. *Phys. B* **2008**, *403*, 4104−4110.
(69) Jasinski, R.; Iob, A. FTIR Measurements of Iron Oxides on Low Alloy Steel. *J. Electrochem. Soc.* **1988**, *135*, 551−556.
(70) Swierk, J. R.; Klaus, S.; Trotochaud, L.; Bell, A. T.; Tilley, D. An Electrochemical Study of the Energetics of Oxygen Evolution Reaction at Nickel Iron (oxy)hydroxide Catalysts. *J. Phys. Chem. C* **2015**, *119*, 19022−19029.
(71) Doyle, R. L.; Godwin, I. J.; Brandon, M. P.; Lyons, M. E. G. Redox and Electrochemical Water Splitting Catalytic Properties of Hydrated Metal Oxide Modified Electrodes. *Phys. Chem. Chem. Phys.* **2013**, *15*, 13737−13783.
(72) Friebel, D.; Louie, M. W.; Bajdich, M.; Sanwald, K. E.; Cai, Y.; Wise, A. M.; Cheng, M.; Sokaras, D.; Weng, T.; Alonso-Mori, R.; Davis, R. C.; Bargar, J. R.; Norshov, J. K.; Nilsson, A.; Bell, A. T. Identification of Highly Active Fe Sites in (Ni,Fe)OOH for Electrocatalytic Water Splitting. *J. Am. Chem. Soc.* **2015**, *137*, 1305−1313.
(73) Fang, Y.-H.; Liu, Z.-P. Mechanism and Tafel Lines of Electro-Oxidation of Water to Oxygen on RuO_2(110). *J. Am. Chem. Soc.* **2010**, *132*, 18214−18222.
(74) Lin, F.; Boettcher, S. W. Adaptive Semiconductor/electrocatalyst Junctions in Water-Splitting Photoanodes. *Nat. Mater.* **2014**, *13*, 81−86.
(75) Trasatti, S. Physical Electrochemistry of Ceramic Oxides. *Electrochim. Acta* **1991**, *36*, 225−241.

DOI: 10.1021/acsami.5b05594
ACS Appl. Mater. Interfaces 2015, 7, 19755−19763